Chinese Chemical Letters 37 (2026) 111345

Contents lists available at ScienceDirect

Chinese Chemical Letters

journal homepage: www.elsevier.com/locate/cclet

Ru-decorated defective tantalum oxide *via* laser synthesis for efficient photothermal CO_2 methanation

Chengxin Liu[a,1], Ying Zhang[a,1], Hui Kong[a], Zizheng Chen[a], Yeshun Zhang[a], Hong Liu[a,b], Wenqiang Gao[a], Kai Zhou[c], Lili Zhao[a,*], Wei Xia[d,*], Xiaoyan Liu[a,*], Weijia Zhou[a,*]

[a] *Institute for Advanced Interdisciplinary Research (iAIR), School of Chemistry and Chemical Engineering, University of Jinan, Ji'nan 250022, China*
[b] *State Key Laboratory of Crystal Materials, Shandong University, Ji'nan 250100, China*
[c] *Center for Advanced Analytical Science, School of Chemistry and Chemical Engineering, Guangzhou University, Guangzhou 510006, China*
[d] *School of Physics and Technology, University of Jinan, Ji'nan 250022, China*

ARTICLE INFO

Article history:
Received 17 March 2025
Revised 30 April 2025
Accepted 19 May 2025
Available online 19 May 2025

Keywords:
Photothermal catalysis
Tantalum oxide
CO_2 methanation
Oxygen vacancy
Laser synthesis

ABSTRACT

The conversion of carbon dioxide (CO_2) into valuable fuels or chemicals through photothermal catalysis is an efficient way to alleviate the global energy crisis and climate change. Regulating active sites and modifying photothermal conversion characteristics are conducive to photothermal catalytic reactions. In this study, the defect-rich tantalum oxide on tantalum foil decorated with Ru nanoparticles (Ru/Ta_2O_{5-x}/Ta) was synthesized using pulsed laser under thermal ablation effects. The presence of oxygen defects enhanced the photothermal conversion efficiency. Meanwhile, the interface between Ru and Ta_2O_{5-x} facilitated the adsorption of CO_2, and Ru nanoparticles served as efficient active sites for the hydrogenation of CO_2 to methane (CH_4). The Ru/Ta_2O_{5-x}/Ta catalyst exhibited excellent photothermal conversion efficiency (reaching 343.4 °C at 1.76 W/cm^2) and excellent catalytic activity with a CH_4 yield of 50.6 mol $g_{(Ru)}^{-1}$ h^{-1} (CH_4 selectivity of 98 %). The experimental and theoretical results demonstrated that the catalytic sites of Ru/Ta_2O_{5-x}/Ta in combination with light irradiation promoted CO_2 activation, intermediate formation and CO* transformation, thereby accelerating the production of CH_4. Moreover, the application of the pulsed laser was extended to construct the photothermal catalyst with high photothermal temperature and efficient catalytic sites.

© 2026 Published by Elsevier B.V. on behalf of Chinese Chemical Society and Institute of Materia Medica, Chinese Academy of Medical Sciences.

With the increased consumption of global fossil fuels and the growing need for sustainability, there are urgent demands for advanced technologies and green materials in the oil and gas industry [1]. As an important part of the "Power-to-Gas (P2G)" system, a hydrogen energy storage technology, photothermal catalytic carbon dioxide (CO_2) methanation can achieve sustainable and clean energy conversion [2,3]. Photothermal catalysis harnesses non-radiative transition or plasmon excitation to concurrently drive both the thermochemical and photochemical processes of the catalyst [4]. This approach not only overcomes the low efficiency in photocatalytic conversion but also decreases the required catalytic reaction temperature for thermal catalysis [5], thus preventing high-temperature sintering and carbon deposition-induced deactivation of the catalyst [6,7]. In this process, regulating active sites and modifying photothermal conversion characteristics contribute to the fabrication of photothermal catalysts with high performance [8]. On the one hand, the active sites required for photothermal catalytic CO_2 methanation are generally transition metals, such as Co, Ni, Rh, Pd, and Ru [8–10]. The catalytic selectivity and activity of the active sites of noble metals are superior to those of non-precious metals [11]. Besides, non-precious metals Ni and Co can lead to deactivation in the reaction process under the action of carbon accumulation [12,13]. Nevertheless, the scarcity of precious metals has hindered their further development. Therefore, it is of great significance to improve the utilization of precious metals [14]. On the other hand, metal nanomaterials can absorb light energy and convert it into heat energy through the local surface plasmon resonance (LSPR) effect, thereby raising the temperature and triggering catalytic reactions. However, the oxide supports are still important not only for dispersing and stabilizing the active metal nanoparticles but also for improving the light utilization efficiency to enhance the photothermal catalytic performance [15,16]. In particular, oxygen vacancies in the oxide supports also affect the adsorption and activation of CO_2 [17].

* Corresponding authors.
E-mail addresses: ifc_zhaoll@ujn.edu.cn (L. Zhao), sps_xiaw@ujn.edu.cn (W. Xia), ifc_liuxy@ujn.edu.cn (X. Liu), ifc_zhouwj@ujn.edu.cn (W. Zhou).
[1] These authors contributed equally to this work.

https://doi.org/10.1016/j.cclet.2025.111345
1001-8417/© 2026 Published by Elsevier B.V. on behalf of Chinese Chemical Society and Institute of Materia Medica, Chinese Academy of Medical Sciences.

Ultrafast synthesis technologies, such as Joule heating [18–20] and Laser synthesis [21–23], are beneficial to the synthesis of nanomaterials with defect structures. As a pollution-free energy source with high energy efficiency, lasers can interact with materials within an extremely short period to achieve heating, melting, vaporization, or phase changes. The high-temperature and high-pressure gas plume region at a small space region formed by laser treatment is prone to induce oxygen vacancy defects [24]. In addition, the unique micro- and nano-integrated structures obtained *via* laser treatment have also garnered significant attention in the catalysis field [25,26]. For example, some scholars performed the laser modulation of oxygen vacancies in TiO_{2-x}/Ti and then anchored single-atom-layer Pt clusters *via* the confinement effect of oxygen vacancies [24]. Besides, the ruthenium-modified catkin-like fluff defect-rich alumina synthesized using ultraviolet (UV) laser showed excellent performance in photothermal conversion and catalytic CO_2 methanation, which could be attributed to the efficient capture of scattered light [27,28] and enhanced light absorption as well as photothermal conversion efficiency [29].

Meanwhile, the anchoring effect of oxygen vacancies can improve the dispersion of the metal active site to form ultra-small Ru nanoparticles and stimulate a strong interaction between the metal and support, thus promoting the catalytic reaction [30,31]. Therefore, the laser construction of defect-rich oxide supports and the anchoring of ultra-small noble-metal catalytic sites as the photothermal catalyst have exhibited certain advantages.

Tantalum oxide (Ta_2O_5) is renowned for its high refractive index and extensive applications in both optical and electronic devices. Owing to the exceptionally high Ta-O bond energy, Ta_2O_5 exhibits remarkable thermodynamic and chemical stability [32,33]. The laser construction of oxygen vacancy defects combined with the high Ta-O bond energy of Ta_2O_5 may play a unique role in the preparation of metal photothermal catalysts supported by defective oxide.

In this study, the defect-rich tantalum oxide on tantalum foil (Ta_2O_{5-x}/Ta) was prepared through laser ablation method. Besides, the Ru nanoparticles were loaded on the surface of Ta_2O_{5-x}/Ta to fabricate the Ru/Ta_2O_{5-x}/Ta catalyst under the thermal effect of lasers and the anchoring effect of oxygen vacancies. For the Ru/Ta_2O_{5-x}/Ta catalyst, the presence of oxygen vacancies enhanced the photothermal conversion efficiency. Meanwhile, the interfaces between Ru and Ta_2O_{5-x} enhanced the adsorption of CO_2, and Ru nanoparticles served as efficient active sites for the hydrogenation of CO_2 to methane (CH_4). The Ru/Ta_2O_{5-x}/Ta catalyst exhibited excellent photothermal conversion efficiency (reaching 343.4 °C at 1.76 W/cm^2) and excellent catalytic activity with a CH_4 yield of 50.6 mol $g_{(Ru)}^{-1}$ h^{-1} (CH_4 selectivity of 98 %). Moreover, the application of the pulsed laser was extended to construct the photothermal catalyst with high photothermal temperature and efficient catalytic sites.

The preparation process of the laser-synthesized Ru/Ta_2O_{5-x}/Ta photothermal catalyst was illustrated in Fig. 1a and Fig. S1 (Supporting information). Owing to the time-saving advantage of the laser processing technique, only 206 s was required for the as-prepared Ta_2O_{5-x}/Ta with a size of 10 mm × 10 mm. The defect-rich Ta_2O_{5-x} was first synthesized on Ta foil by the laser ablation process. The high-temperature and high-pressure vapor plume reacted with the ambient gas during laser treatment, which contributed to the generation and retention of oxygen vacancies. The formation of blue-black (rather than white) tantalum pentoxide in Fig. 1b verified the presence of many oxygen vacancies, and the Ta foil was argenteous. The electron paramagnetic resonance (EPR) results (Fig. S2 in Supporting information) also confirmed the presence of oxygen vacancies in Ta_2O_{5-x}/Ta at $g = 2.004$. The image of field emission scanning electron microscopy (FESEM) in Figs. 1c and d showed that Ta_2O_{5-x}/Ta had a catkin-like fluff micro/nanostructure,

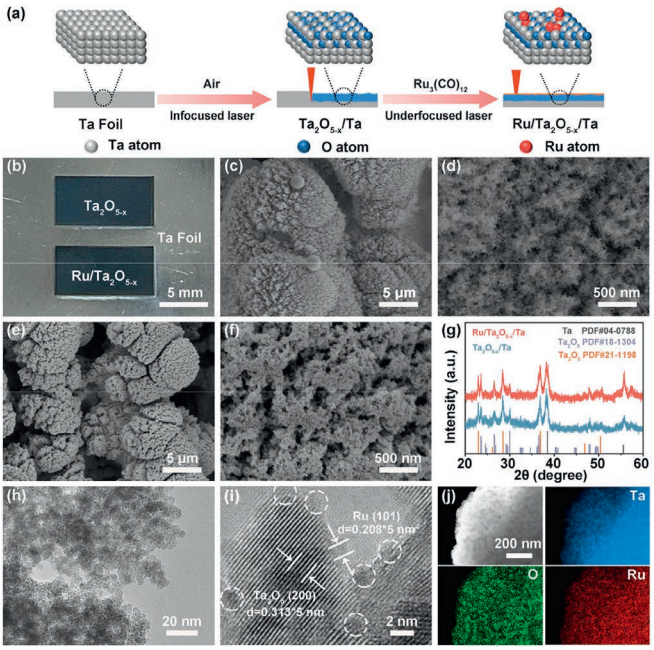


Fig. 1. (a) Schematic illustration of the laser synthesis of Ru/Ta_2O_{5-x}. (b) Optical photograph of Ta_2O_{5-x} and Ru/Ta_2O_{5-x} on Ta foil. SEM images of (c, d) Ta_2O_{5-x}/Ta and (e, f) Ru/Ta_2O_{5-x}/Ta. (g) XRD patterns of Ta_2O_{5-x}/Ta and Ru/Ta_2O_{5-x}/Ta. (h, i) HRTEM images and (j) according EDS mapping of the Ru/Ta_2O_{5-x}/Ta.

which could efficiently trap the light and minimize light dissipation. The cross-section FESEM image in Fig. S3 (Supporting information) showed that the thickness of the laser-prepared Ta_2O_{5-x} was ~101 μm. As shown in Fig. 1a, after the ruthenium carbonyl was dropped on the laser-prepared Ta_2O_{5-x}/Ta, the thermal effect of lasers in the under-focus mode was employed to decompose $Ru_3(CO)_{12}$ into Ru with the catalyst presenting black color (Fig. 1b). The oxygen vacancies as anchoring sites, along with laser thermal decomposition, promoted the production of Ru nanoparticles. As illustrated by the FESEM images in Figs. 1e and f, the addition of Ru did not destroy the primitive micro/nanostructure of Ta_2O_{5-x}/Ta. The X-ray powder diffraction (XRD) results in Fig. 1g revealed that the miscible tantalum pentoxide composed of the hexagonal Ta_2O_5 (PDF #18–1304) with the diffraction peak at 22.9°, 28.3°, 36.8°, and 50.4° corresponding to (003), (200), (203), and (200) crystal faces and the triclinic Ta_2O_5 (PDF #21–1198) with the diffraction peak at 23.5°, 26.5°, 29.9°, and 36.5° corresponding to (101), ($\bar{1}$05), (0012), and (1$\bar{1}$6) crystal faces were obtained. Except for the detected main diffraction peak for Ta_2O_5, the other diffraction peaks at 38.5° (110) and 55.6° (200) of Ta (PDF #04–0788) were also detected. The results indicated that the miscible structure of tantalum pentoxide was successfully constructed by lasers on the Ta foil. Of note, the Ru content in Ru/Ta_2O_{5-x}/Ta was not detected by XRD due to the ultra-low loading but by inductively coupled plasma (ICP) spectroscopy (Table S1 in Supporting information), which was 0.015 wt%.

To verify the formation of Ru-decorated Ta_2O_{5-x}, the structure of the scraped Ru/Ta_2O_{5-x} samples was further analyzed using transmission electron microscopy (TEM). The flocculent morphology and Ru particles with higher contrast dispersed on Ta_2O_{5-x} were observed (Fig. 1h). The Ru nanoparticles with a diameter of approximately 2 nm were ascribed to the oxygen vacancies within Ta_2O_{5-x}, which served as anchoring sites and prevented the nanoparticles from agglomeration. High-resolution transmission electron microscopy (HRTEM) of Fig. 1i and Fig. S4 (Supporting information) showed the presence of Ta_2O_5 with lattice spacings of 0.313 nm and 0.377 nm, respectively. These two crys-

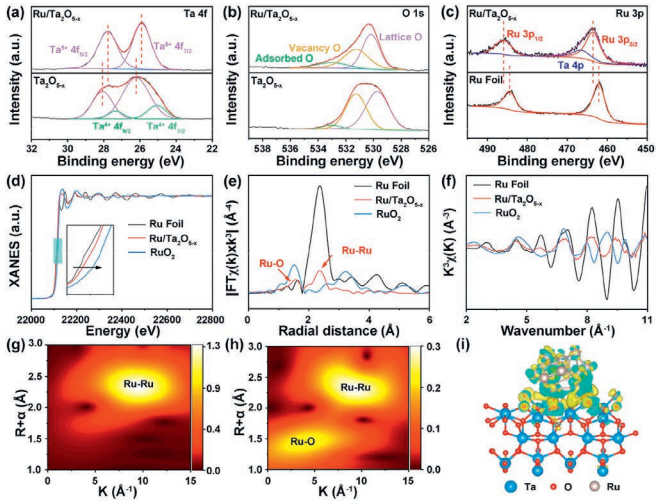


Fig. 2. High-resolution XPS spectra of (a) Ta 4f and (b) O 1s for Ta_2O_{5-x}/Ta and Ru/Ta_2O_{5-x}/Ta. (c) Ru 3p XPS spectra of Ru/Ta_2O_{5-x}/Ta and Ru foil. (d) Normalized Ru K-edge XANES spectra. (e) Fourier transform of k^3-weighted Ru EXAFS spectra and (f) the k^3-weighted EXAFS signals of Ru foil, Ru/Ta_2O_{5-x}/Ta and RuO_2. WT-EXAFS of the Ru foil (g) and Ru/Ta_2O_{5-x}/Ta (h). (i) Difference charge density of Ru/Ta_2O_{5-x}/Ta (the yellow region represents the electron accumulation, while the green region represents the electron depletion).

tal planes correspond to the (200) crystal plane of hexagonal Ta_2O_5 and the (101) crystal plane of triclinic Ta_2O_5, respectively. Additionally, the lattice fringe of 0.208 nm was associated with the (101) crystal plane of Ru. Furthermore, the aggregation of Ru nanoparticles was not observed. The energy-dispersive spectroscopy (EDS) elements mapped in Fig. 1j showed a uniform distribution of Ta, O, and Ru, which further validated the successful preparation of the Ru/Ta_2O_{5-x} composite.

The electronic properties of Ru/Ta_2O_{5-x}/Ta were investigated by X-ray photoelectron spectroscopy (XPS) (Figs. 2a-c). The XPS survey spectra of Ru/Ta_2O_{5-x}/Ta were characterized by the presence of Ru, Ta, and O (Fig. S5 in Supporting information). The Ta 4f spectrum (Fig. 2a) of Ta_2O_{5-x}/Ta prepared by laser ablation could be deconvolved into two component peaks, which were attributed to Ta^{4+} at 27.34 and 25.07 eV and Ta^{5+} at 28.07 and 26.22 eV, respectively. After the decoration using Ru nanoparticles, only the XPS peaks corresponding to Ta^{5+} at 27.78 and 25.90 eV were observed. The disappearance of the Ta^{4+} peak intensity in Ru/Ta_2O_{5-x}/Ta was ascribed to the anchoring of Ru, which then consumed the oxygen vacancies in the laser thermal decomposition process. Additionally, the Ta^{5+} peaks were shifted to lower binding energy (27.78 and 25.90 eV) in Ru/Ta_2O_{5-x}/Ta compared with that of Ta_2O_{5-x}/Ta (28.07 and 26.22 eV), indicating the electron transfer from Ru to Ta_2O_{5-x}. In terms of the O 1s spectrum in Fig. 2b, three peaks assigned to the adsorbed oxygen (O_{ad}), lattice oxygen (O_L), and oxygen vacancy (O_V) at 533.01, 529.72, and 531.25 eV were detected for Ta_2O_{5-x} [35–37]. After the decoration using Ru nanoparticles on Ta_2O_{5-x}/Ta, the vacancy oxygen was consumed, implying the anchoring effect of these oxygen vacancies. As shown in Fig. 2c, the Ru 3p spectrum of Ru/Ta_2O_{5-x}/Ta revealed that the binding energy was 463.54 eV for the Ru $3p_{3/2}$ peak and 485.87 eV for the Ru $3p_{1/2}$ peak, respectively, suggesting the formation of metallic Ru by thermal decomposition and the anchoring effect of oxygen vacancies. Compared with Ru foil (462.10 and 484.40 eV), the XPS peak of Ru shifted to higher binding energy in Ru/Ta_2O_{5-x}/Ta, further implying the electron transfer from Ru to Ta_2O_{5-x}. This result was consistent with that of Ta^{5+} 4f (Fig. 2a). All the above results demonstrated the successful synthesis of Ru/Ta_2O_{5-x}/Ta and the establishment of a strong interaction between Ta_2O_{5-x} supports and Ru.

The X-ray absorption near-edge structure (XANES) spectra and extended X-ray absorption fine structure (EXAFS) spectra were observed to identify the valence states and local coordination structure of Ru/Ta_2O_{5-x}/Ta. As shown in Fig. 2d, the Ru K-edge XANES spectrum revealed that Ru/Ta_2O_{5-x}/Ta possessed similar characteristics to Ru foil. Combined with the FT-EXAFS spectrum (Fig. 2e), a significant peak corresponding to Ru-Ru scattering and a weak Ru-O bond could be observed, indicating that Ru^0 was the predominant species in the sample. The detailed structural parameters are summarized from the curve fitting in Table S2. Furthermore, when amplifying the edge energy of Ru/Ta_2O_{5-x}/Ta and Ru foil (inset in Fig. 2d), the Ru K-edge in Ru/Ta_2O_{5-x}/Ta shifted to slightly higher energy compared with that of Ru foil. This suggested a higher average valence state of Ru in Ru/Ta_2O_{5-x}/Ta. This observation aligned with the XPS results (Fig. 2c). Fig. 2f displayed the k^3-weighted EXAFS signals. Ru/Ta_2O_{5-x}/Ta at low wavenumbers showed a slightly advanced phase relative to Ru foil, revealing different surrounding scatters of Ru atoms in Ru/Ta_2O_{5-x}/Ta. The Ru K-edge WT-EXAFS of Ru/Ta_2O_{5-x}/Ta and Ru foil displayed in Figs. 2g and h illustrated that an evident WT signal corresponding to the Ru-Ru bond in the K (~10 $Å^{-1}$) and $R+\alpha$ (~2.5 Å) position was detected. This further validated the loading of Ru nanoparticles on Ta_2O_{5-x}/Ta. Additionally, Ru-O bond signals were also detected in Ru/Ta_2O_{5-x}/Ta due to the Ru-O interaction between Ru^0 and the Ta_2O_{5-x}/Ta support (Fig. 2h, Figs. S6 and S7 in Supporting information). The differential charge density of Ru/Ta_2O_{5-x}/Ta supported this conclusion (Fig. 2i and Fig. S8 in Supporting information). Due to the difference in electronegativity, the accumulation of electrons at Ta_2O_{5-x}/Ta was observed, indicating that electrons transferred from Ru to Ta_2O_{5-x}/Ta. This further revealed a strong interaction between Ru and Ta_2O_{5-x}/Ta, thereby enhancing the catalytic performance within the system.

The light absorption capacity was quantified using UV–vis absorption spectroscopy to investigate the photothermal properties of Ru/Ta_2O_{5-x}/Ta (Fig. 3a). As a wide band gap semiconductor material (~4.0 eV), Ta_2O_{5-x}/Ta exhibited its intrinsic absorption edge at 310 nm. Meanwhile, due to the light trapping effect of the micro/nanostructures and the presence of oxygen vacancies, favorable light absorption of Ta_2O_{5-x}/Ta in the full spectral range was revealed. After Ru was loaded on Ta_2O_{5-x}/Ta, the catalyst exhibited slightly enhanced adsorption throughout the UV–vis wavelength range, thereby establishing a solid foundation for photothermal conversion, which was crucial for photothermal catalysis. Subsequently, the photothermal conversion efficiency of Ta_2O_{5-x}/Ta and Ru/Ta_2O_{5-x}/Ta was evaluated. The photothermal temperatures and infrared thermal images recorded at 1.76 W/cm^2 were presented in Figs. 3b and c. The accuracy of the temperature measurements was confirmed by thermocouples and consistent results obtained from the infrared camera (Tables S3 in Supporting information). The surface temperature of the laser-synthesized Ta_2O_{5-x}/Ta catalyst increased sharply to 195.7 °C under irradiation. Notably, Ta_2O_{5-x} with different photothermal conversion temperatures can be obtained by controlling the processing power of the laser (Figs. S9 and S10 in Supporting information). After the decoration using Ru nanoparticles, the photothermal temperature of Ru/Ta_2O_{5-x}/Ta was further increased to 222.7 °C. This further demonstrated that the incorporation of Ru improved the absorbance of Ru/Ta_2O_{5-x}/Ta (Fig. 3a), thereby increasing the photothermal conversion of this catalyst. Of note, when subjected to identical irradiation conditions, the surface temperature of the Ru metal was only 76.2 °C, implying that the primary photothermal conversion temperature of Ru/Ta_2O_{5-x}/Ta was provided by defective tantalum oxide (Fig. S11 in Supporting information). By comparing the photothermal properties of laser-prepared Ru/Al_2O_{3-x}, Ru/TiO_{2-x} and Ru/Ta_2O_{5-x}, among them, Ru/Ta_2O_{5-x} showed more excellent light-absorbing ability, which was conducive to obtaining better

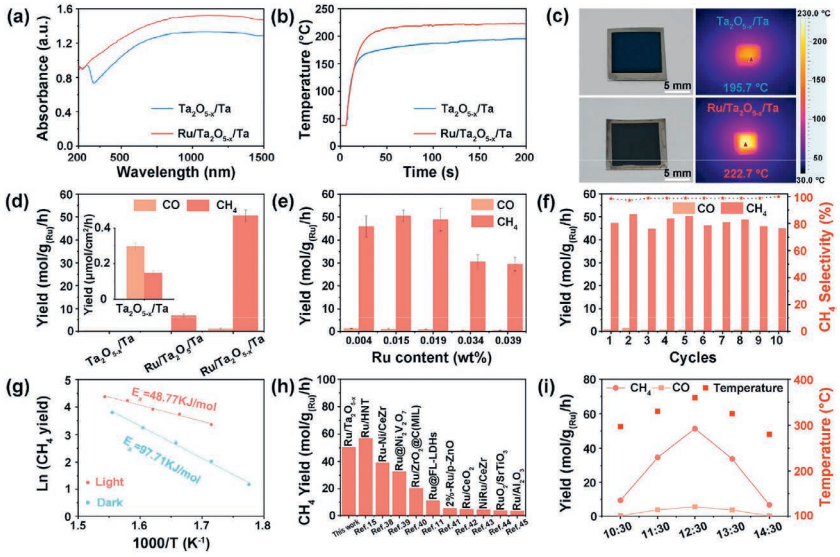


Fig. 3. (a) UV–vis absorption spectra, (b) photothermal temperature curves and (c) corresponding infrared thermal images of Ta_2O_{5-x}/Ta and Ru/Ta_2O_{5-x}/Ta. (d) Catalytic performances of Ta_2O_{5-x}/Ta, Ru/Ta_2O_5/Ta and Ru/Ta_2O_{5-x}/Ta (The inset represents the CH_4 and CO yields of Ta_2O_{5-x}/Ta). (e) Catalytic performance of Ru/Ta_2O_{5-x}/Ta with different Ru loadings. (f) Cycle stability test of the Ru/Ta_2O_{5-x}/Ta (testing conditions: CO_2:H_2 = 1:4, initial reactor pressure = 0.1 MPa, light intensity = 1.76 W/cm^2). (g) The Arrhenius plot with activation energies of Ru/Ta_2O_{5-x}/Ta in the photothermal and thermal catalysis. (h) Catalytic efficiency comparison of photothermal CO_2 to CH_4 conversion for Ru/Ta_2O_{5-x}/Ta to other literature. (i) The production rate of the Ru/Ta_2O_{5-x}/Ta as a function of time under ambient sunlight irradiation (Experiments conducted in Ji'nan, Shandong Province, 11 August 2024).

photothermal catalytic performance (Figs. S12-S14 in Supporting information).

To identify the catalytic sites of Ru/Ta_2O_{5-x}/Ta for CO_2 methanation, the photothermal catalytic CH_4 yields of Ta_2O_{5-x}/Ta and Ru/Ta_2O_{5-x}/Ta were calculated. As illustrated in Fig. S15 (Supporting information), the thermal insulation characteristic was enhanced by the incorporation of aluminosilicate fibers, resulting in a decreased thermal conductivity of Ru/Ta_2O_{5-x}/Ta. Ru/Ta_2O_{5-x}/Ta was placed in a 200 mL reactor for the catalytic reaction (Fig. S16 in Supporting information). As shown in Fig. 3d, Ta_2O_{5-x}/Ta was hardly active for CO_2 hydrogenation toward CH_4. Only a small amount of CO (0.297 μmol cm^{-2} h^{-1}) was produced. Although oxygen vacancies in Ta_2O_{5-x}/Ta facilitated the activation of CO_2, the insufficiency of effective H_2 dissociation sites limited the subsequent hydrogenation process. Conversely, after the introduction of Ru species into the Ta_2O_{5-x}/Ta system, a notable increase in the production of CH_4 was observed, suggesting that the Ru species acted as efficient active sites for the CO_2 methanation reaction. Notably, as shown in Fig. 3e and Fig. S17 (Supporting information), the production of CH_4 per unit area of Ru/Ta_2O_{5-x}/Ta gradually increased with an increase in the loading amount of Ru. However, the mass activity of CH_4 production decreased with an increase in the content of Ru, which was attributed to the increasingly enhanced particle aggregation effect with an increase in the loading amount of Ru (Fig. S18 in Supporting information), which reduced the utilization of Ru [34]. The optimal catalytic performance of Ru/Ta_2O_{5-x}/Ta reached 50.6 mol $g_{(Ru)}^{-1}$ h^{-1} at the Ru loading amount of 0.015 wt%. To verify the role of oxygen vacancies in Ru/Ta_2O_{5-x}/Ta during photothermal catalysis, these oxygen vacancies were reduced by calcining laser-synthesized Ru/Ta_2O_{5-x}/Ta in air. As shown in Fig. S19 (Supporting information), the XRD patterns showed that the phase component of the sample did not change after calcination. The EPR results (Fig. S20 in Supporting information) validated the consumed oxygen vacancies after calcination. However, the photothermal temperature of Ru/Ta_2O_5/Ta did not show a significant difference. Fig. 3d showed that the corresponding CH_4 yield also decreased after the oxygen vacancies were reduced (7.03 mol $g_{(Ru)}^{-1}$ h^{-1} under 1.76 W/cm^2). This suggested that oxygen vacancies promoted photothermal catalysis by serving as anchoring sites and improved photothermal temperature. The cycle stability test results of Ru/Ta_2O_{5-x}/Ta in Fig. 3f displayed that there was no noticeable performance degradation over the ten cycles, proving higher stability. Furthermore, the structural stability of Ru/Ta_2O_{5-x}/Ta was also verified by the morphology and structure characterization after the photothermal stability test (Figs. S21-S23 in Supporting information). The UV–vis-NIR absorption spectra (Fig. S24 in Supporting information) indicated that Ru/Ta_2O_{5-x}/Ta retained high optical absorption performance after the cycle stability test.

To further clarify the role of light and photothermal temperature, the temperature and CH_4 yield of Ru/Ta_2O_{5-x}/Ta at different optical power densities were explored in a batch reactor (Fig. S25 in Supporting information). The results showed that the photothermal temperature and CH_4 yield increased with an increase in the light intensity. To draw a comparison, the thermocatalytic reaction at corresponding temperatures was also carried out in the dark. The results showed that the CH_4 yield and selectivity of Ru/Ta_2O_{5-x}/Ta in the photothermal system were superior to those in the pure thermal system (Figs. S25 and S26 in Supporting information). The Arrhenius plots of the photothermal and thermal systems in Fig. 3g showed that the activation energy of photothermal catalysis (48.77 kJ/mol) was lower than that of thermal catalysis (97.71 kJ/mol), which indicated that the introduction of light could significantly decrease the activation energy through a photochemical effect. The photogenerated charge transfer significantly diminished the reaction energy barrier for key intermediates in the CO_2 methanation process, thereby accelerating the reaction rate. In addition, when cooling water was used to exclude the thermal effect under light exposure, a sharp decrease in CH_4 yield was detected to only 0.24 mmol $g_{(Ru)}^{-1}$ h^{-1} (Fig. S27 in Supporting information). This demonstrated that the thermal effect induced by light exposure was also crucial in this photothermal catalytic reaction.

To assess the photothermal catalytic efficiency of Ru/Ta_2O_{5-x}/Ta, the CH_4 yields per unit of Ru from recently published photothermal catalysts were presented in Fig. 3h and Table S4 (Supporting information). The CH_4 yield normalized to Ru for

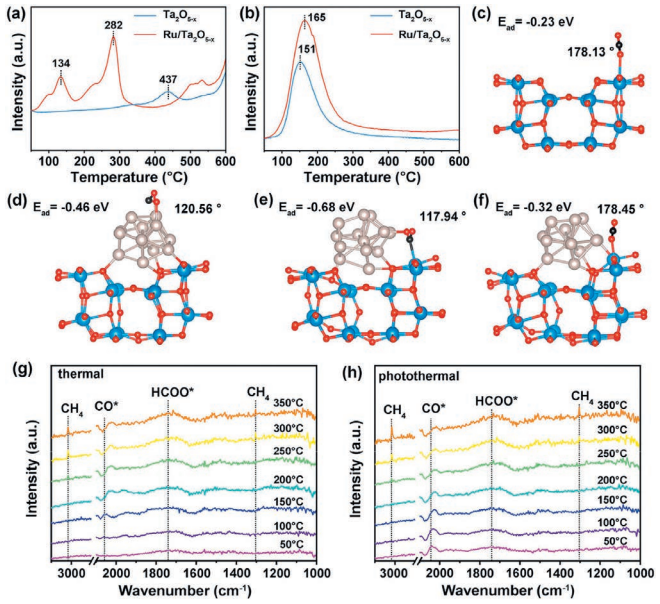


Fig. 4. (a) H_2-TPR and (b) CO_2-TPD comparison profiles of the Ta_2O_{5-x}/Ta and Ru/Ta_2O_{5-x}/Ta. Optimized structures of CO_2 molecules adsorbed on the surface of (c) Ta_2O_{5-x}, (d) Ru nanoparticles, (e) Ru and Ta_2O_{5-x} interfaces and (f) Ta_2O_{5-x} in Ru/Ta_2O_{5-x}. *In-situ* DRIFTS spectra measured during CO_2 methanation over the Ru/Ta_2O_{5-x}/Ta at different temperatures (g) under dark conditions and (h) under solar illumination.

Ru/Ta_2O_{5-x}/Ta was superior to or comparable to such reported catalysts as Ru/HNT (56.8 mol $g_{(Ru)}^{-1}$ h^{-1}) [15], 0.5Ru-10Ni/CeZr(AcAc) (39.2 mol $g_{(Ru)}^{-1}$ h^{-1}) [38], Ru@$Ni_2V_2O_7$ (32.8 mol $g_{(Ru)}^{-1}$ h^{-1}) [39], Ru/ZrO_2@C(MIL) (20.45 mol $g_{(Ru)}^{-1}$ h^{-1}) [40], Ru@FL-LDHs (11.1 mol $g_{(Ru)}^{-1}$ h^{-1}) [11], 2 %Ru-ZnO (5.4 mol $g_{(Ru)}^{-1}$ h^{-1}) [41], Ru/CeO_2 (4.64 mol $g_{(Ru)}^{-1}$ h^{-1}) [42], NiRu/CeZr (4.5 mol $g_{(Ru)}^{-1}$ h^{-1}) [43], RuO_2/$SrTiO_3$ (3.7 mol $g_{(Ru)}^{-1}$ h^{-1}) [44], and Ru/Al_2O_3 (3.4 mol $g_{(Ru)}^{-1}$ h^{-1}) [45]. Even in the comparison of the area activity of these catalysts, the production rate (2.943 mmol cm^{-2} h^{-1}) of Ru/Ta_2O_{5-x}/Ta was still superior to or comparable to the reported catalysts (Table S5 in Supporting information). These results corroborated the superior intrinsic catalytic activity of Ru/Ta_2O_{5-x}/Ta. Finally, to demonstrate the practical application of Ru/Ta_2O_{5-x}/Ta, the photothermal catalytic system composed of a catalyst, a Fennel lens, aluminosilicate fiber wool, and a quartz reactor was constructed under the outdoor sunlight (Fig. S28 in Supporting information). After the reaction gas was injected into the reaction system, the yield of CO and CH_4 was recorded from 10:30 to 14:30. The results presented in Fig. 3i demonstrate that the CH_4 production rate initially increases and subsequently decreases with time progression, reaching 51.4 mol $g_{(Ru)}^{-1}$ h^{-1} at 12:30. This observation confirms the sustained excellent catalytic activity of Ru/Ta_2O_{5-x}/Ta even under natural sunlight conditions.

The H_2 temperature-programmed reduction (H_2-TPR) and CO_2 temperature-programmed desorption (CO_2-TPD) were further employed to investigate the absorption and activation behavior of the Ru/Ta_2O_{5-x}/Ta catalyst for H_2 and CO_2, respectively. As shown in Fig. 4a, Ta_2O_{5-x}/Ta possessed the weak H_2 reduction peak at 437 °C, which can be attributed to the inert substrates. The TPR profile of Ru/Ta_2O_{5-x}/Ta displayed two unsymmetrical peaks centered at 134 °C and 282 °C, respectively, which appeared at lower temperatures compared with that of Ta_2O_{5-x}/Ta due to efficient dissociation of H_2. In terms of CO_2-TPD (Fig. 4b), Ta_2O_{5-x}/Ta and Ru/Ta_2O_{5-x}/Ta possessed similar peak positions and significant signals, indicating that Ta_2O_{5-x}/Ta provided the activation of CO_2 to a certain degree due to the presence of oxygen vacancies. Of note, the higher CO_2 adsorption peak areas after Ru loading for Ru/Ta_2O_{5-x}/Ta implied that the stronger absorption ability of CO_2 molecules might be attributed to the construction of the interface between Ru nanoparticles and Ta_2O_{5-x}. To identify whether the heterogeneous interfaces were active sites for CO_2 adsorption, the calculation based on the first-principles density functional theory (DFT) was conducted to investigate the adsorption and activation characteristics of CO_2. As shown in Figs. 4c-f and Fig. S29 (Supporting information), the adsorption energy (E_{ad}) and O=C=O bond angles of CO_2 were calculated by the optimized CO_2 adsorption geometry on Ta_2O_{5-x} and Ru/Ta_2O_{5-x}. Distinctly, the E_{ad} of CO_2 at the interface between Ru and Ta_2O_{5-x} was more negative (−0.68 eV) than that on the Ta_2O_{5-x} surface (−0.32 eV) and Ru nanoparticles (−0.46 eV). This demonstrated that the heterogeneous interface between Ru and Ta_2O_{5-x} was a more efficient adsorption site for CO_2 molecules. Upon the catalytic adsorption of CO_2, the subsequent activation was initiated, which could be revealed by the changes in the O=C=O bond angle [46]. As depicted, the changes in the O=C=O bond angle at the interface between Ru and Ta_2O_{5-x} were also more significant than those on the surface of Ru and Ta_2O_{5-x} in Ru/Ta_2O_{5-x}. This further validated the effect of the heterogeneous interface on accelerating CO_2 activation. The above theoretical calculation results were consistent with the CO_2-TPD results in Fig. 4b, demonstrating the construction of interfaces between Ru and Ta_2O_{5-x} could further enhance the adsorption and activation of CO_2 based on the oxygen vacancies of Ta_2O_{5-x}.

To clarify the CO_2 to CH_4 reaction pathway and the effect of light on the reaction, *in-situ* diffuse reflectance infrared Fourier transform spectroscopy (*in-situ* DRIFTS) experiments were performed to detect the production of intermediates. As shown in Figs. 4g and h, the peak at 1741 cm^{-1} was attributed to HCOO* [46,47]. The peak observed at 2058 cm^{-1} corresponded to the adsorption peak of CO* on Ru, indicating that chemically adsorptive CO species were formed during CO_2 methanation [48,49]. Notably, the adsorption peak of CO* on Ru gradually shifted with an increase in temperature, indicating the occurrence of CO* hydrogenation on Ru [50,51]. Through a comparative analysis between dark and illuminated conditions, it was found that there was no significant difference in the variety of surface intermediates detected, suggesting a similar reaction pathway for both photothermal and thermal CO_2 hydrogenation. Compared with thermal catalysis (Fig. 4g), photothermal catalysis (Fig. 4h) showed adsorption peaks of CO* on Ru as low as 50 °C. This indicated that the introduction of light could effectively activate CO_2 [49], which was consistent with the results in Fig. 3g. When the temperature was above 250 °C, the strong signals at 1305 cm^{-1} and 3016 cm^{-1} were ascribed to the C—H stretching vibrations of CH_4. Notably, under light irradiation conditions (Fig. 4h), an increase in the CH_4 signal coincided with a decrease in the CO* absorption band, indicating that CO* species play a key role as intermediates in the production of CH_4. This finding also revealed that the introduction of light was beneficial to accelerating the conversion of CO*, thereby promoting the formation of CH_4. From the above analysis, a possible reaction pathway for the photothermal hydrogenation of CO_2 on Ru/Ta_2O_{5-x}/Ta was identified. Firstly, CO_2 molecules were adsorbed and activated on both Ta_2O_{5-x} and the interface between Ru and Ta_2O_{5-x}. Meanwhile, the H_2 molecule was chemically dissociated on Ru, thus producing atomic hydrogen species. The produced H* migrated and reacted with the activated CO_2* species to form HCOO*, which was then decomposed into CO* and H_2O ($CO_2 \rightarrow CO_2^* \rightarrow HCOO^* \rightarrow CO^*$). Following this, CO* species underwent further hydrogenation at the Ru sites. This process resulted in the formation of transient intermediates such as CHO* and CH_3O*, which were the pivotal intermediates in the production of CH_4 ($CO^* \rightarrow CHO^* \rightarrow CH_2O^* \rightarrow CH_3O^* \rightarrow CH_4$). Through the comparative analysis based on dark and illuminated conditions, light

irradiation facilitated CO_2 activation, intermediate formation, and CO^* transformation, eventually promoting the production of CH_4.

Overall, the Ru-decorated defective tantalum oxide on Ta foil ($Ru/Ta_2O_{5-x}/Ta$) was successfully prepared using the laser ablation method, and the catalyst was then applied to the photothermal catalytic CO_2 methanation reaction. The high-temperature and high-pressure gas plume region within a small space formed by laser treatment facilitated the generation and preservation of oxygen defects, and the presence of oxygen defects successfully anchored the Ru nanoparticles on Ta_2O_{5-x}/Ta. In addition, the unique micro- and nano-integrated structures obtained *via* laser treatment also garnered significant attention in the catalysis field. On the one hand, the laser-prepared Ta_2O_{5-x}/Ta structure increased the photothermal conversion temperature under light illumination, which facilitated the photothermal catalytic reaction. On the other hand, the oxygen vacancies acted as anchoring sites to anchor and disperse Ru nanoparticles. With the addition of Ru nanoparticles as efficient active hydrogenation sites to CH_4, the interface between Ru and Ta_2O_{5-x} served as the adsorption and activation sites of CO_2 molecules. Therefore, $Ru/Ta_2O_{5-x}/Ta$ exhibited higher photothermal conversion efficiency (reaching 343.4 °C at 1.76 W/cm^2) and enhanced catalytic activity with a CH_4 yield of 50.6 mol $g_{(Ru)}^{-1}$ h^{-1} (CH_4 selectivity of 98%). The *in-situ* DRIFTS spectra indicated that light irradiation accelerated CO_2 activation and promoted CH_4 formation.

CRediT authorship contribution statement

Chengxin Liu: Writing – original draft, Validation, Investigation. **Ying Zhang:** Writing – review & editing, Supervision. **Hui Kong:** Writing – review & editing, Methodology. **Zizheng Chen:** Writing – review & editing, Investigation. **Yeshun Zhang:** Writing – review & editing, Investigation. **Hong Liu:** Writing – review & editing, Resources, Methodology. **Wenqiang Gao:** Writing – review & editing, Conceptualization. **Kai Zhou:** Writing – review & editing, Conceptualization. **Lili Zhao:** Writing – review & editing, Conceptualization. **Wei Xia:** Writing – review & editing, Resources, Methodology. **Xiaoyan Liu:** Writing – review & editing, Resources. **Weijia Zhou:** Writing – review & editing, Methodology, Investigation, Funding acquisition, Formal analysis.

Declaration of competing interest

The authors declare that they have no known competing financial interests or personal relationships that could have appeared to influence the work reported in this paper.

Acknowledgments

This work was supported by the Taishan Scholar Project of Shandong Province (No. tstp20240515), the Natural Science Foundation of Shandong Province (Nos. ZR2021JQ15, ZR2022YQ42, ZR2020LLZ006), the Innovative Team Project of Jinan (No. 2021GXRC019) and the National Natural Science Foundation of China (Nos. 52102171, 52472097).

Supplementary materials

Supplementary material associated with this article can be found, in the online version, at doi:10.1016/j.cclet.2025.111345.

References

[1] M. Li, X. Liu, K. Lv, et al., Prog. Mater. Sci. 139 (2023) 101187.
[2] S. Fang, Y.H. Hu, Chem. Soc. Rev. 51 (2022) 3609–3647.
[3] X. Cui, Q. Ruan, X. Zhuo, et al., Chem. Rev. 123 (2023) 6891–6952.
[4] Z. Li, J. Liu, R. Shi, et al., Adv. Energy Mater. 11 (2021) 2002783.
[5] L. Yuan, M.Y. Qi, Z.R. Tang, et al., Angew. Chem. Int. Ed. 60 (2021) 21150–21172.
[6] F. Zhang, Y.H. Li, M.Y. Qi, et al., Chem. Catal. 1 (2021) 272–297.
[7] C. Sun, Z. Zhao, H. Liu, et al., Rare Met. 41 (2022) 1403–1405.
[8] Z. Wang, Z. Yang, Z.C. Kadirova, et al., Coord. Chem. Rev. 473 (2022) 214794.
[9] X. Meng, T. Wang, L. Liu, et al., Angew. Chem. Int. Ed. 53 (2014) 11478–11482.
[10] G. Chen, R. Gao, Y. Zhao, et al., Adv. Mater. 30 (2017) 1704663.
[11] J. Ren, S. Ouyang, H. Xu, et al., Adv. Energy Mater. 7 (2016) 1601657.
[12] A. Parastaev, V. Muravev, E. Huertas Osta, et al., Nat. Catal. 3 (2020) 526–533.
[13] M. Monai, K. Jenkinson, A.E.M. Melcherts, et al., Science 380 (2023) 644–651.
[14] J. Kong, S. Song, W. Zhao, et al., Appl. Catal. B: Environ. 339 (2023) 123118.
[15] K. Peng, J. Ye, H. Wang, et al., Appl. Catal. B: Environ. 324 (2023) 122262.
[16] A. Tavasoli, A. Gouda, T. Zähringer, et al., Nat. Commun. 14 (2023) 1435.
[17] Y. Qi, L. Song, S. Ouyang, et al., Adv. Mater. 32 (2019) 1903915.
[18] W. Zhang, X. Wei, T. Wu, et al., Nano Energy 118 (2023) 108994.
[19] J. Luo, J. Zhang, Z. Guo, et al., Adv. Mater. 36 (2024) 2405956.
[20] S. Zhu, Q. Xu, C. Guan, et al., Nano Lett. 2 (2025) 4c05097.
[21] X. Liu, T. Zhang, M. Xu, et al., Nano Res. 17 (2023) 1578–1584.
[22] J. Bian, L. Zhou, X. Wan, et al., Adv. Electron. Mater. 5 (2019) 1800900.
[23] F.C. Wang, Z.B. Guo, Z.Y. Wang, et al., Adv. Mater. 35 (2023) 2210038.
[24] D. Jiang, H. Yuan, Z. Liu, et al., Appl. Catal. B: Environ. 339 (2023) 123081.
[25] W.J. Kang, Y. Feng, Z. Li, et al., ACS Energy Lett. 8 (2023) 3512–3519.
[26] W. Yu, J. Yu, M. Huang, et al., Energy Environ. Sci. 16 (2023) 2991–3001.
[27] S.C. Singh, M. ElKabbash, Z. Li, et al., Nat. Sustain. 3 (2020) 938–946.
[28] X. Liu, C. Xing, F. Yang, et al., Adv. Energy Mater. 12 (2022) 2201009.
[29] W. Wei, Z. Wei, R. Li, et al., Nat. Commun. 13 (2022) 3199.
[30] X. Guo, C. Dong, M. Gao, et al., Appl. Catal. B: Environ. 341 (2024) 123286.
[31] Y. Ding, J. Chen, X. Lian, et al., Appl. Catal. B: Environ. 343 (2024) 123508.
[32] Z. Wen, Y. Song, H. Shi, et al., J. Energy Storage 98 (2024) 113037.
[33] L. Liu, C. Liu, M.Y. Wang, et al., Rare Met. 42 (2023) 2957–2971.
[34] Z. Chen, X. Dong, Z.X. Sun, et al., ACS Nano 18 (2024) 19672–19681.
[35] A. Ourefelli, A. Hajjaji, K. Trabelsi, et al., Chem. Eng. J. 468 (2023) 143769.
[36] X. Yu, J. Zhao, J. Huang, et al., J. Colloid Interface Sci. 572 (2020) 141–150.
[37] X. Yu, Z. Li, J. Liu, et al., Appl. Catal. B: Environ. 205 (2017) 271–280.
[38] S. Renda, A. Ricca, V. Palma, Appl. Energy 279 (2020) 115767.
[39] Y. Chen, Y. Zhang, G. Fan, et al., Joule 5 (2021) 3235–3251.
[40] D.S. Alqarni, C.W. Lee, G.P. Knowles, et al., Catal. Today 371 (2021) 120–133.
[41] W. Liao, C. Tang, H. Zheng, et al., J. Catal. 407 (2022) 126–140.
[42] J.A.H. Dreyer, P. Li, L. Zhang, et al., Appl. Catal. B: Environ. 219 (2017) 715–726.
[43] E. le Saché, L. Pastor-Pérez, B.J. Haycock, et al., ACS Sus. Chem. Eng. 8 (2020) 4614–4622.
[44] D. Mateo, J. Albero, H. García, Joule 3 (2019) 1949–1962.
[45] A. Quindimil, U. De-La-Torre, B. Pereda-Ayo, et al., Catal. Today 356 (2020) 419–432.
[46] C. Guo, Y. Tang, Z. Yang, et al., ACS Nano 17 (2023) 23761–23771.
[47] P. Liu, Y.L. Men, X.Y. Meng, et al., Angew. Chem. Int. Ed. 62 (2023) e202309443.
[48] X. Lin, K. Yang, R. Si, et al., Appl. Catal. B: Environ. 147 (2014) 585–591.
[49] X. Li, J. Lin, L. Li, et al., Angew. Chem. Int. Ed. 59 (2020) 19983–19989.
[50] F. Wang, S. He, H. Chen, et al., J. Am. Chem. Soc. 138 (2016) 6298–6305.
[51] S. Deng, Z. Qian, C. Zhu, et al., ACS Catal. 14 (2024) 16508–16521.